Erasmus Mundus Master in Image Processing and Computer Vision

MSc Thesis

3D Modeling of Tissue Deformation for Ultrasound Simulation

Presented at

Université de Bordeaux

Author: Hermosilla Campos, Blanca

Supervisors: PARASHAR Shaifali and BASARAB Adrian

Date: June, 2024

Declaration of Authenticity

I, the undersigned Blanca Hermosilla Campos, student of the Image Processing and Computer Vision MSc program, hereby declare that I have prepared the present thesis myself, without any unauthorized help, and that I have only used the sources specified in the thesis. I have clearly marked all parts that I have literally taken from other sources or have rewritten or translated while keeping the meaning of the original text, also indicating the source thereof.

I declare that I have not submitted this thesis to any other higher education institutions, excluding the partner universities of the IPCV Consortium.

Blanca Hermosilla Campos

Abstract

Ultrasound imaging is widely used in the clinical practice mainly due to its real-time and non-invasive capabilities. The advancement of ultrasound technology relies heavily on robust simulation methods to test and refine new algorithms. Ultrasound simulation encompasses the generation of radiofrequency (RF) data emitted by transducers and the subsequent generation of B-mode images through post-processing techniques.

Current ultrasound simulation methods, predominantly overlook tissue deformation. Most of them operate under the assumption of static tissue scatterers arranged in a non-deformed, regular grid configuration. This limitation undermines the accuracy and realism of the simulated ultrasound images, as real-world imaging scenarios involve some degree of tissue displacement due to the pressure exerted by the ultrasound probe.

This work explores the application of the Finite Element Method (FEM) to model tissue displacement caused by the ultrasound probe's force. This displacement is then used to update tissue scatterers reflecting their position in a post- deformed configuration. We integrate the scatterer model proposed by Gaits el al.(2023) [1] with 3D FEM simulation to obtain ultrasound images accounting for tissue deformation. Tissues are modeled using elasticity principles, and characterized by mechanical properties (Young's Modulus and Poisson Ratio). Recognizing that tissues do not deform in one single dimension when compressed, we propose the use of an augmented Acquisition Zone to account for scatterer displacement out of the imaging plane, and a subsequent spatial filtering with the probe's Acquisition Zone post-deformation. The final B-mode image is generated using the convolutional approach.

We leverage FEniCS software [1] to define the variational form describing the tissue deformation under the probe's pressure. FEniCS automates the FEM process, allowing us to efficiently solve the governing equations and obtain the displacement field. Furthermore, it grant access to different powerful tools, that have facilitated the deformation modeling in the simulation framework.

Acknowledgements

I would like to thank my supervisors Shaifali Parashar and Adrian Basarab, for providing me with the opportunity to pursue my internship at Creatis and Liris research laboratories, and for their guidance and support throughout the internship period. I would also like to thank the PhD student François Gaits, for his assistance and willingness to answer my questions regarding his previous work. Last but not least, I thank my family and friends for their unconditional support during my master's years away from home.

Contents

Chapter 1

Introduction

1.1. Ultrasound Imaging Fundamentals

Ultrasound imaging modality is widely used in clinical practice due to its low-cost, real-time capability and non-invasive, non-destructive evaluation of tissues. An ultrasound examination consists of moving a transducer over the patient's body to scan 3D internal organs. It generates 2D cross-sectional images of the anatomy being examined, based on the probe's position and angle.

The fundamental physics of ultrasound involves the propagation of high frequency sound waves (1-20 MHz) produced by a transducer that converts electrical energy into mechanical energy and vice versa. As ultrasound waves travel through the tissues, they encounter boundaries between different materials of varying acoustic impedance, causing partial reflection and transmission of the waves. Reflections of the sound waves that return to the probe are known as *echoes*. The more significant the difference in the density of the two tissues, the stronger the echo will be produced, resulting in a hyperechoic (brighter) image. The opposite occurs when there is a small difference in density between tissues, resulting in a hypoechoic (darker) image.

Tissues reflect ultrasound waves differently depending on their interfaces and microstructure composition. Smooth interfaces are considered *specuclar reflectors* resulting in sound waves being reflected back in relatively uniform directions. On the other hand, irregular interfaces are called *diffuse reflectors* causing the scattering of ultrasound waves in different directions. A particular type of scatter, known as Rayleigh scattering, occurs when reflectors' surfaces are much smaller than the beam's wavelength. These small reflectors are known as *scatterers*[2].

As a result of the interference of the scattered waves, the typical noise pattern known

as ultrasonic *speckle* is formed. When multiple scattered waves overlap, they can either interfere constructively or destructively, resulting in different patterns that can provide valuable information about tissue microstructure. Nevertheless, although informative, speckles can also be seen as noise compromising tissue contrast and image quality.

When the transducer receives echo signals, it generates raw electrical signals known as RF (radio frequency) data, which contain detailed amplitude and phase information. To create ultrasound images, a process called beamforming combines the RF signals from multiple transducer elements. The beamformed signals undergo a series of post-processing steps, including envelope detection, log compression, and filtering. Finally, a grayscale image, known as B-mode, is produced where pixel brightness corresponds to echo signal strength.

Understanding ultrasound physics and the intricacies of speckle formation is not only crucial for interpreting clinical images but also plays a significant role in the development of ultrasound simulators. The growing interest in simulation technology extends beyond physician training to test new computational algorithms in controlled settings. To enhance realism in ultrasound simulation, it is essential to accurately capture both speckle patterns and tissue deformation induced by the compression of the probe during an ultrasound examination.

1.2. Ultrasound Simulation

A critical step for ultrasound simulation is to model echos resulting from the interactions between the ultrasound waves and the different volume elements constituting the tissue sample i.e. *scatterers*. In this context, mammalian cells within a specific type of tissue are assumed to act as weak point scatterers with identical scattering power, simplifying the complexity of interactions and allowing for a more straightforward simulation of the echo formation process [3]. Figure 1.1, shows an example of a simulated echocardiographic image from a collection of scatterers mimicking the anatomy of the heart.

Wave-based approaches simulate ultrasound propagation in tissue by solving complex acoustic wave equations. Common physical simulators in the literature include Field II [4] or Simus [5]. These can yield highly accurate and realistic results in static images. The main drawback of these simulations is the high computational time required. On the other hand, *convolution-based* methods are capable of producing realistic ultrasound speckle patterns while decreasing the computational time, making them more suitable for
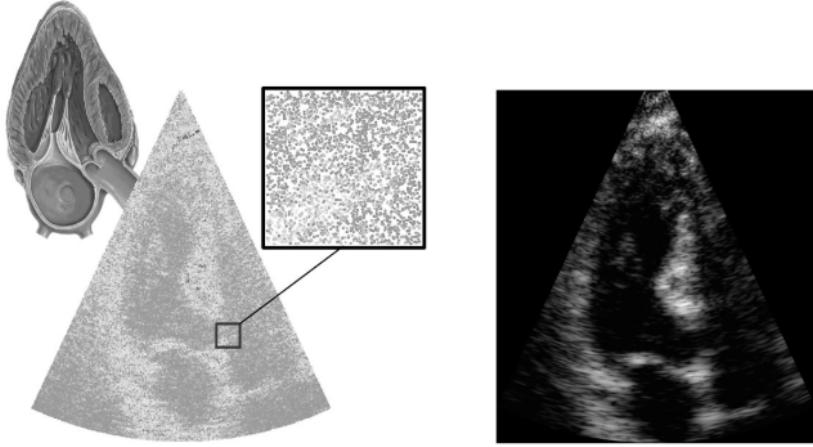
Figure 1.1: Simulated three-chamber-view echocardiographic image, generated by SIMUS using ∼40,000 scatters (left). Taken from [12]

real-time applications. Notably, the simulation model proposed by Meunier and Bertrand has been widely used [6], wherein the interaction between ultrasound field and tissue is approximated as the convolution of tissue scatterers with an ultrasound system spatial impulse response (point-spread function, PSF) [7]. Additionally, *ray-tracing* methods have emerged as promising approaches from real-time simulations simulating the interaction of ultrasound waves with scatterers using techniques from derived from computer graphics and physics-based modeling [8].

Tissue scatterers are typically modeled as a collection of points with varying amplitudes and spatial positions. The amplitude of the scatterers is often represented by a Gaussian distribution, allowing tissue characterization to be quantified by the mean and the standard deviation, the latter representing tissue's structural heterogeneity which is related to the scattered strength of the returning echoes [9],[10]. A common approach to generate scatterers' amplitudes involves scaling random values drawn from a standard normal distribution $N(0, 1)$ using the tissue-specific standard deviation [4]. The collection of these standard deviations forms a representative map of the tissues to be simulated, commonly referred to as *scattering strength map* or *tissue mimicking map* [4][11].

Regarding the spatial distribution of the scatterers, one of the main challenges arises from the need to ensure a uniform coverage of the tissue sample volume to be simulated. Some authors proposed the use of a rectangular grid, potentially with minor random perturbations, or opting for a completely random distribution [3]. The generation and storage of a sufficiently large number of scatterers is essential to ensure a fully developed speckle. When transitioning from 2D to 3D ultrasound simulation there is a significant

14

increase in the required number of scatters, which escalates from thousands to tens or hundreds of billions for 3D volumes [11]. Consequently, the storage and manipulation of such vast quantities requires advanced strategies to manage these computational demands efficiently.

1.3. Soft Tissues Deformation

Soft tissue modeling spans various research domains, including medical simulations, character animations, or cloth deformation in 2D and virtual try-ons in the fashion industry [13],[14],[15]. From a biomechanical point of view, tissue modeling consists of predicting the behaviour of deformable tissues in response to applied forces or displacements.

Soft tissues can be regarded as composite, non-homogeneous, more or less incompressible, non-linear viscoelastic materials [16]. Despite this complexity, certain assumptions are made to facilitate modeling. These include treating tissue as linear elastic for small deformations, isotropic and nearly incompressible. Specifically, this means that the resulting strain increases linearly with incremental stress, the tissue returns to its original (non-deformed) state after the load is removed, the tissue responds uniformly to stress, and its overall volume remains nearly constant under applied stress [16]–[18]. Building on these assumptions, the theory of elasticity establishes the foundation framework to formulate the mechanical dynamics of the tissues under force application using the laws of *continuum mechanics*.

At the heart of continuum mechanics lie the fundamental concepts of deformation and displacement, which are introduced to measure the change in position and shape within a solid body. As illustrated in Figure 1.2, a material point X in the reference configuration is displaced to a material point x in the deformed configuration, guided by the deformation function $\Phi : R^3 \to R^3$. This function maps points X to x via $\Phi(X) = X + u(X)$ with $u(X)$ representing the *displacement*. In the same way, a straight line on the reference configuration will be mapped to a smooth curve on the deformed configuration. The *deformation gradient* F describes how an infinitesimal line segment dX, is stretched and rotated, with $dx = FdX$ representing the resulting change [19].

From the deformation gradient F, different geometric measurements can be derived. Starting with the *Green-Lagrange strain tensor* $E(x)$, defined as:

$$E(x) = \frac{1}{2}\left[(F^\top F)(x) - I\right] \tag{1.1}$$
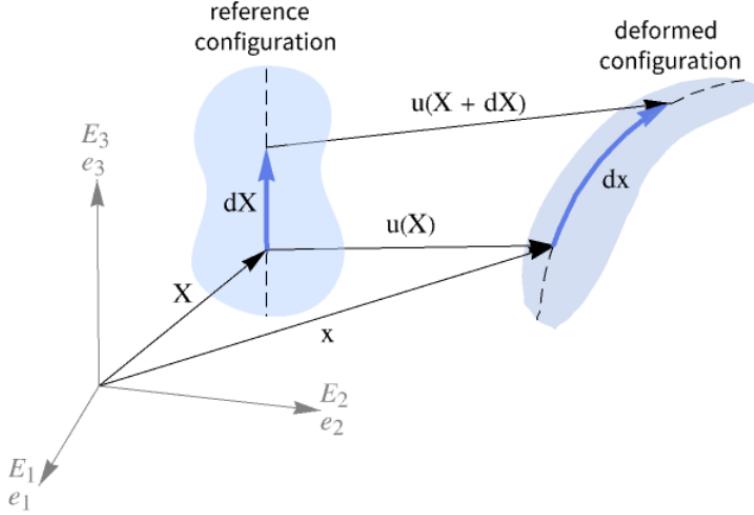
Figure 1.2: Reference configuration and deformed configuration of a continnum body [19].

where I is the identity matrix. When $\Phi(x)$ is a rigid-body motion, $E(x) = 0$, indicating no strain. As a result, the Green-Lagrange strain tensor measures how much a given displacement locally differs from a rigid-body displacement [20]. In the context of small deformations, the *infinitesimal strain tensor*, denoted as $\epsilon(u)$ is often used. It serves as an approximation that simplifies the mathematical analysis of the deformation by assuming that the displacements and rotations involved are sufficiently small to neglect non-linear effects. The infinitesimal strain measure is given by:

$$\epsilon(u) = \frac{1}{2}(\nabla(u) + (\nabla(u)^\top)$$ (1.2)

In addition to measuring deformation, it is crucial to understand how internal forces are generated as resistance when an elastic body is exposed to external loads. The stress at a point within the body is described by the *stress tensor* $\sigma(x)$. It can be described as a function of the infinitesimal strain ϵ and thus, the displacement u thought the constitutive equation, which is also known as the *material model*:

$$\sigma = \lambda \mathrm{tr}(\varepsilon)I + 2\mu\varepsilon$$ (1.3)

where λ, and μ are the *Lamé constants*. These constants characterize the material response to deformation and are fundamental in determining its mechanical behaviour. They can be calculated from commonly known material properties such as Young's modulus (E) and Poisson's ratio (ν), as follows:

$$\lambda = \frac{E\nu}{(1+\nu)(1-2\nu)} \quad , \quad \mu = \frac{E}{2(1+\nu)}$$ (1.4)

16

No material properties are used in the derivation of the equilibrium equation since they are applicable to any material. The equilibrium equation is given by:

$$f + \nabla \cdot \sigma = 0 \tag{1.5}$$

Linear elastic deformations can be effectively modeled with appropriate boundary conditions and equations including kinematic, constitutive, and balance equations, as described in (1.2), (1.3), and (1.5), respectively. Using measured values of Young's Modulus and Poisson's Ratio reflecting the biomechanical properties of the tissue being modeled is crucial. Young's modulus provides a measure of stiffness, while Poisson's Ratio measures tissue compressibility. Figure 1.3 illustrates the Young's modulus for different tissues within the human body, allowing their characterization based on mechanical properties. Additionally, tissue stiffness plays a significant role in differentiating between diseased and healthy regions within the tissue, as pathological changes often alter the mechanical behavior of tissues. Accounting for these mechanical differences has proven valuable in tumor detection [21].
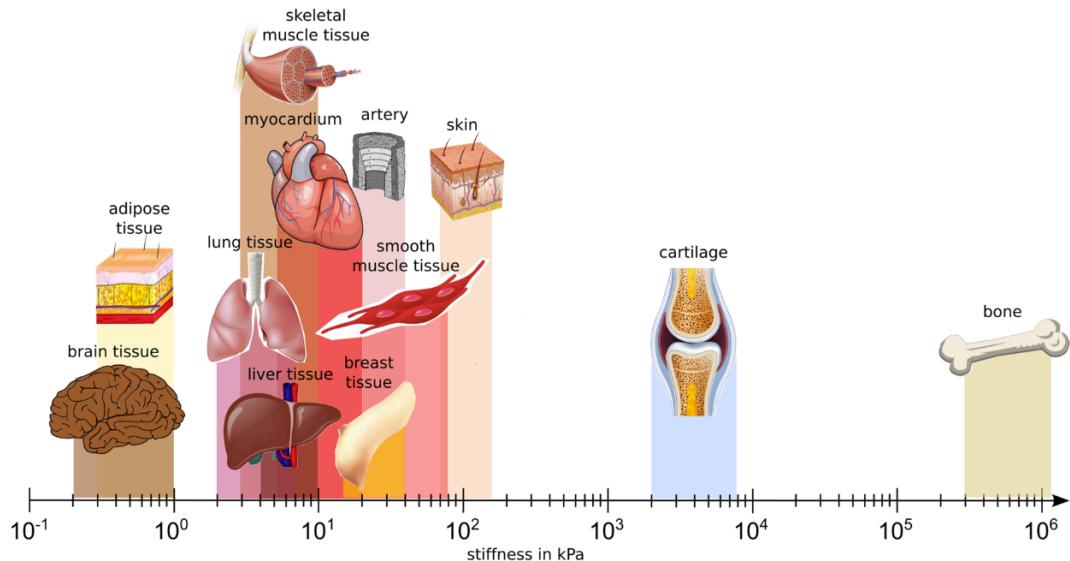
Figure 1.3: Mechanical properties of different human tissues. Taken from [22]

The mechanics of biological soft tissues can be effectively simulated with finite element models [23]. The Finite Element Method (FEM) plays a crucial role in biomechanics and engineering by enabling the simulation of real-world deformations and facilitating the understanding of tissue responses under diverse loading conditions. It involves discretizing the continuous domain of soft tissue into smaller, simpler elements to form a finite element mesh. Each element approximates the tissue's mechanical behavior based on

17

defined constitutive laws. Within these elements, interpolation functions, are utilized to interpolate values from discrete node points, ensuring smooth transitions across the mesh. This approach treats soft tissues as continuous materials, allowing complex mechanical behaviors to be accurately approximated over simple element shapes rather than the entire problem domain.

1.4.   Contributions

This thesis work builds upon the work proposed by Gaits et al. (2023) [11], titled "Efficient Stratified 3D Scatterer Sampling for Freehand Ultrasound Simulation". Their methodology is used as a foundation for the scatterer extraction with respect to a probe's position and a tissue mimicking volume in a reference (non-deformed) configuration.

- **Deformation-aware scatterer placement.** This contribution involves integrating the deformation effects induced by the probe-tissue interaction. By incorporating principles from the theory of linear elasticity and using the Finite Element Method (FEM), the displacement field resulting from tissue deformation is calculated. Subsequently, scatterers' positions are updated with respect to the deformed configuration, thereby enhancing the realism of the simulation.

- **Enhanced tissue mimicking volume.** This work extends the concept of tissue mimicking maps to incorporate the biomechanical properties of the medium. By integrating parameters such as Young's Modulus and Poisson ratio into the tissue mimicking volume, a more comprehensive representation of tissue behaviour is achieved. This enables the simulation of a wider range of tissue types.

- **Expansion of numerical phantom capabilities.** This work extends the capabilities of numerical phantoms by enabling the creation of a collection of geometric objects (cube, sphere, plane), rather than just single objects. This extension can open the door to more flexible and realistic representations of anatomical structures in the future.

1.5.   Outline

The summary of the chapters of the thesis work:

Chapter 2 This chapter provides a review of related works, focusing on the applications of the FEM and the integration of deformation modeling into ultrasound simulation frameworks.

Chapter 3 This chapter presents the integration of FEM simulation and scatterer model into the simulation framework. It reviews the mathematical foundation and the implementation using FEniCS software.

Chapter 4 This chapter showcases results of simulated ultrasound images accounting for tissue deformation, contrasting them with non-deformed simulated images. ParaView software is used to visualize the effects of the deformation in different tissue samples in the 3D domain.

Chapter 5 This chapter offers a summary of findings, reflecting on conclusions drawn from the results and suggesting new lines for future work.

Chapter 2

Related Works

2.1.   Soft Tissue Simulation

Surgical simulations have been among the pioneering applications of soft tissue deformation modeling in the medical field, aiming to assist surgeons in planning optimal surgical strategies and enhancing their training. Both traditional and robot-assisted surgeries require extensive training for surgeons to proficiently perform procedures. While anatomical models created from the reconstruction of acquired image data constitute a well-established research area, surgical simulations require sophisticated methods to simulate how soft tissues deform in response to interactions with tools such as needles, scalpels, or ultrasound probes.

Soft tissue modeling in medical simulations must achieve both realism and real-time performance. To ensure realism, soft tissue models must accurately represent the deformability of actual tissues. This accuracy depends on the choice of mathematical models, which can vary according to the type of tissue being modeled. For instance, from the systematic review of real-time medical simulations carried out by [24], works in literature commonly model skin as either a linear elastic or hyperelastic material, breast tissue as hyperelastic, liver tissue as nonlinear elastic, and blood vessels as viscoelastic materials.

Due to the real-time computational demands of surgical simulations, most existing methods use elastic constitutive law to describe soft tissue deformation. This is the simplest way to model the mechanical response of soft tissues for most materials. However, it is only valid for small displacements. For large displacements, more complex non-linear models should be considered to capture the true behaviour of the tissues accurately [25]. It's important to note that while more complex constitutive laws can enhance fidelity, they

also introduce greater computational overhead, which may pose challenges for achieving real-time performance in medical simulations.

2.2. FEM Simulations in Ultrasound

The literature review on the estimation of tissue deformation using FEM simulations in ultrasound reveals three main purposes:
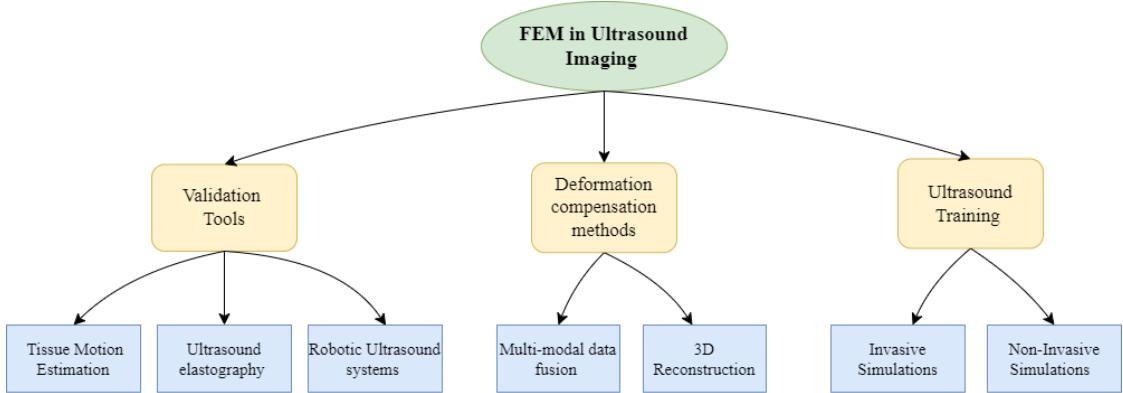
Figure 2.1: Conceptual Map: FEM applications in Ultrasound Imaging.

Validation Tools

To validate novel algorithms, a priori knowledge is necessary, which can be accessed through simulations. In [26],[27] simulated RF data accounting for tissue motion was used to evaluate blood velocity estimators, stationary echo canceling filters, and other filters for processing recorded RF-signals. Simulations with tissue motion provided prior knowledge of tissue components in the RF signal; blood and surrounding tissue. Separating these components is essential for accurate blood velocity estimation. Their models included tissue motion induced by pulsation, heartbeat, and breathing, derived from in vivo RF data using autocorrelation methods between adjacent RF lines. In order to estimate RF data with tissue deformation, point scatterers with amplitude properties of tissue or blood, were moved around according to the motion model and fed into the RF simulation program Field II.

Similarly, in response to the need for experimental evaluation of strain estimation methods, FEM simulations were employed to generate post-compression RF data. In contrast to inherent tissue motion, these simulations applied a uniform compression load to the top of the tissue while keeping the bottom fixed, also known as quasi-static defor-

mation. In these experiments, researchers typically constructed both homogeneous and non-homogeneous incompressible phantoms with known mechanical properties.

Early works such as [28], used FEM to model 2D axial compression, while [29] extended the simulation to various degrees of axial compressions in 3D. Later works, such as those by [30] using FEM from ANSYS-11 software and [31] using ABAQUS software package, further advanced 3D axial compression modeling. Field II is widely recognized as the preferred ultrasound simulation software in these studies, utilizing a linear elastic model for tissues.

Moreover, FEM simulations were crucial in controlled experiments using phantoms to validate non-invasive imaging of Young's modulus and Poisson's ratio from estimated axial and lateral strains in vivo. Imaging the mechanical properties of tissues has gained significant interest due to its potential to detect pathological conditions based on biomechanical property alterations. [32] used 3D FEM simulations with commercial ABAQUS, employing both linear elastic and poroelastic tissue models to enhance understanding and accuracy in tissue characterization through non-invasive imaging techniques.

More recently, FEM has been proposed as a validation tool to assess the performance of emerging imaging technologies, such as robotic ultrasound systems [33].

Deformation Compensation Methods

Deformation, although realistic in ultrasound simulations, can also be viewed as an artifact that complicates fusion with other modalities or patient 3D models derived from imaged anatomy. Addressing this use, [34] used 3D FEM simulation to estimate deformation caused by the known surface geometry of the probe contact area. A distinguishing feature of their work is the use of tetrahedral meshes with finer elements near the superficial central region where probe contact occurs to accurately simulate local high-strain deformations. The displacement field obtained with FEM is then used to undo the deformation at the voxel intensity level.

Ultrasound Training

Medical training in ultrasound is essential because low signal-to-noise ratios and imaging artifacts can complicate interpretation for diagnostics. Additionally, invasive procedures such as biopsy training, brachytherapy, and catheter placement require proficient ultrasound skills. Computer simulations can create and integrate relevant content into a repeatable learning environment, making even rare pathologies easily accessible.

Current ultrasound simulators assume a static, non-deformed configuration of a 3D volume, which can be obtained from ultrasound or other modalities like CT. In ultrasound training, simulators commonly involve reslicing and post-processing techniques to include deformations. However, these simulations do not account for tissue motion, which is a significant limitation.

One approach to incorporate deformation, is to first compute the deformed voxel locations and then find (interpolate) the pixel intensities. However, it has a major disadvantage: the deformed voxels no longer lie on a regular-grid structure, making interpolation techniques difficult. To overcome this limitation, [35] proposed an inverse deformation mapping of image pixel locations in 2D back to the pre-deformed volume 3D configuration. The position of the pixels are located within a deformed mesh in 3D using the FEM. Each 3D pixel location in the deformed configuration is then interpolated to the regularly spaced undeformed pixel locations. This method allows for simple and fast interpolation techniques on a regular-spaced grid. Deformation was applied by indenting a phantom with the probe, fixing nodes at the bottom of the phantom, and applying displacement constraints on the nodes in contact with the probe. Using trilinear interpolation (TLI), the simulation of a B-mode frame on the same computer took approximately 25 ms.
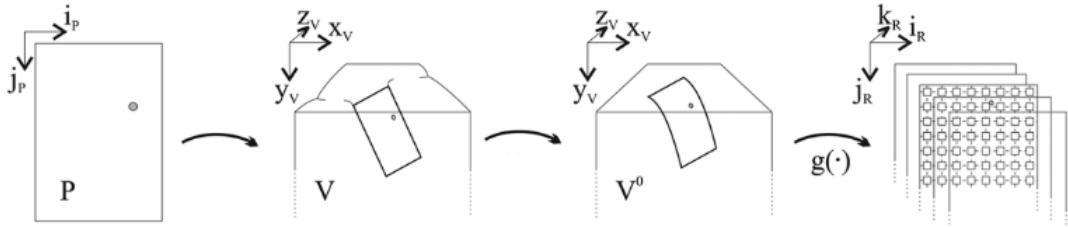
Figure 2.2: Transformation that maps a pixel to the reference voxel volume, where interpolation g(·) finds its intensity value. From Goksel et al. (2009) [35]

The inverse deformation mapping idea was also used by [36] and its subsequent work [37]. In these cases, they used ray-tracing techniques to simulate B-mode ultrasound images, including deformation. To handle deformation, they proposed working in the scatterer domain. The amplitude of the scatterers is derived from the voxel image in the deformed configuration, computed using inverse deformation and interpolation techniques. They also introduced the feasibility of dynamic simulations by fusing low-interest areas (background) with animated anatomical models. This can simulate heart motion or variations of fetuses at all gestational ages, where surrounding tissue (background) deforms accordingly to create space for the fetus.

For invasive simulations, models for needle-deformable tissue interaction have been widely studied in the literature. More recent methods, propose the use FE models to simulate lacerations around the needle [38].

2.3. Conclusion

After this review, we have identified two main possibilities to handle tissue deformation in ultrasound simulation using the FEM. Firstly, *at scatterer level*, which is commonly found in validation techniques that use FEM simulation to obtain a priori information about RF data accounting for displacement induced either by tissue intrinsic motion or compression forces. However, these methods terminate at the simulation of RF data; they are not commonly applied for end-to-end simulation of B-mode ultrasound images.

On the other hand, deformation at *voxel level* is used for interpolative simulations which are often used for medical training. Starkov et al. (2019) [37] also adopt this approach, utilizing ray-tracing techniques to handle deformation within the scatterer domain. Instead of physically relocating scatterers to simulate post-deformation configurations, this method updates scatterer amplitudes using inverse deformation and interpolation of voxel intensity values. While effective for generating B-mode images with deformation, this approach assumes a constant number and distribution of scatterers within regular cell grids post-deformation, which may not always hold true. An opportunity for future research could lie in fully integrating the deformation process into the scatterer domain, no matter the ultrasound simulation technique employed.

Chapter 3

Ultrasound Simulation with Tissue Deformation

In this thesis, we explore the simulation of ultrasound B-mode images with tissue deformation induced by the pushing force of an ultrasound probe. Figure 3.1 illustrates the workflow for the proposed simulation framework. Purple rectangles indicate the processes taken from previous work by Gaits et al. (2023) [11], which includes a scatterer model and other processes related to the generation of the B-mode image following the convolutional approach. Blue rectangles correspond to the processes designed to include deformation into the simulation flow, which mainly involve a deformation model using FEM, and other processing functions to apply the deformation field to the scatterers' positions, resulting in a post-deformation frame. We propose the use of an augmented Acquisition Zone (AZ) to extract the scatterers in order to account for their possible movement in the x, y, and z directions, and subsequent filtering within the probe's AZ in the post-deformation configuration. Further details are explained in the next subsections.
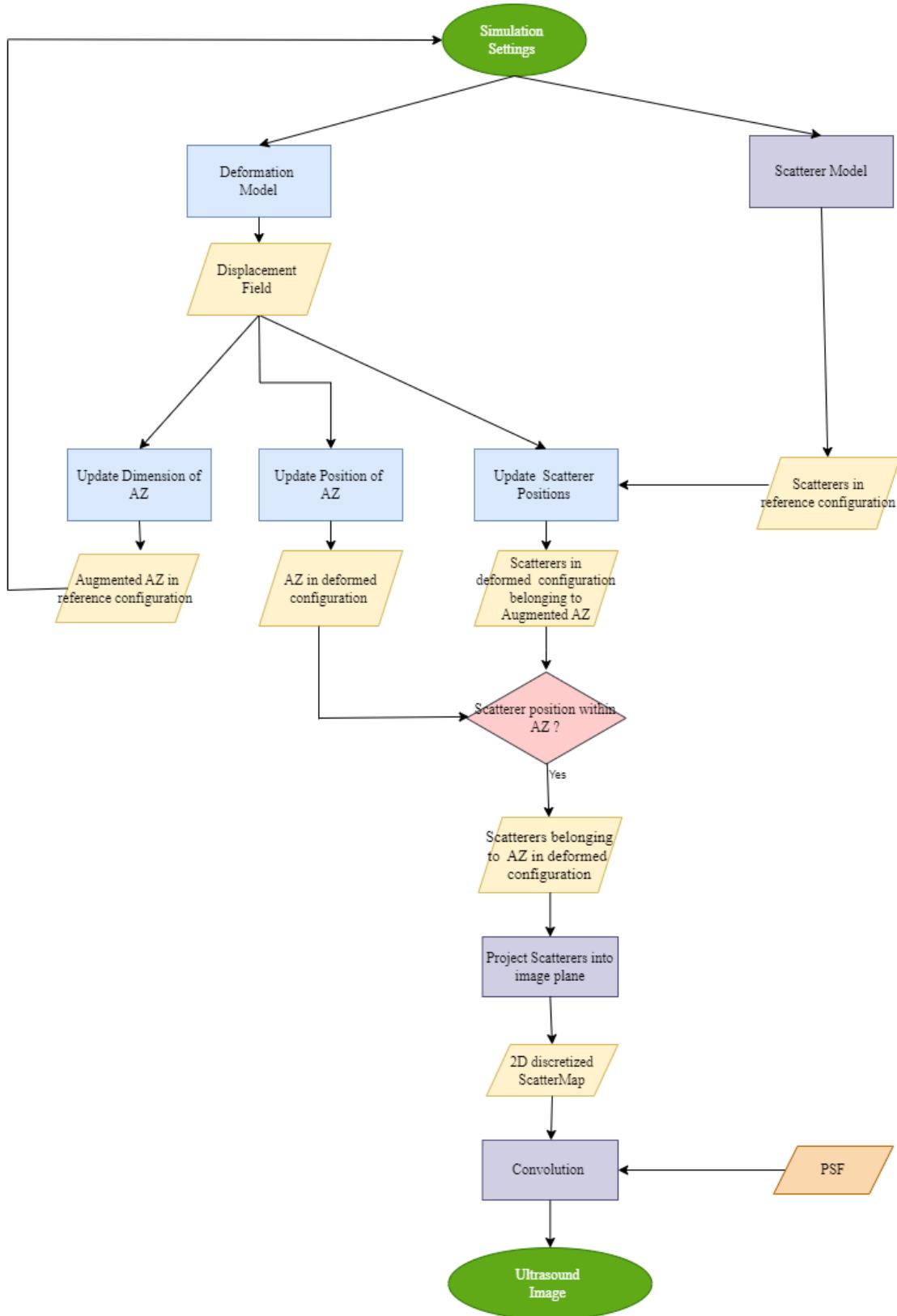
Figure 3.1: Workflow of the proposed simulation methodology, integrating previous processes from Gaits et al.(2023) for scatterer extraction and B-mode image generation (purple) with new processes for deformation modeling using FEM and scatterer adjustment post-deformation (blue).

3.1. Spatially Coherent Ultrasound Simulation (SCUS)

Gaits et al. introduce a novel approach for 3D scatterer generation, emphasizing a memory-efficient data structure that minimizes storage requirements while ensuring rapid scatterer access. Here we present the main aspects of their approach, which serve as the foundational scatter model in our simulation framework.

3.1.1 Scatterer Generation

Scatterer generation is structured around a grid data approach, where a tissue volume is organized into regular cells, each containing a predetermined number of scatterers. This method minimizes computational demands by storing only the scatterer positions within one cell, instead of the whole population. They employ stratified sampling to ensure uniform distribution while mitigating aliasing through random perturbations like rotations. The spatial distribution within cells is crucial, they propose the use of constant random sequences based on discrepancy and blue-noise sampling, specifically DT or Cascaded Sobol. Therefore, per each cell, only a perturbation index, the position of the cell, and a seed of the random sequence need to be stored. Scatterer amplitudes are defined with respect to a tissue mimicking volume. Random numbers are drawn from a standard normal distribution N (0, 1) using the cell random seed, and scaled by its value sampled at its position from the tissue mimicking volume.

3.1.2 Scatterer Extraction

Scatterers within a defined AZ are extracted from a grid-based volume. Firstly, the AZ is characterized as a rectangular parallelepiped, determined by the probe's width, height, and depth, with position and orientation dictated by the probe's location. Then, the scatterer extraction becomes a projection of the scatter points to the probe coordinate system. Given $S_{Gr} = (S_{Gr_x}, S_{Gr_y}, S_{Gr_z})$ the scatterer position in the grid coordinate system, its projection in the probe coordinate system, denoted by $S_{AZ} = (S_{AZ_x}, S_{AZ_y}, S_{AZ_z})$, is given by:

$$S_{AZ} = (S_{Gr} - T_a) \times R_a^{-1}$$

where T_a and R_a represent the translation and rotation of the probe, respectively. Spatial hashing is utilized to efficiently identify cells within the AZ, ensuring that only those intersecting or included within the AZ are considered for scatterer extraction. Additionally, a slightly bigger acquisition zone is used to ensure the detection of partially included

cells.

3.1.3 Implementation Overview

The SCUS simulation framework is implemented in C++ and can be executed using the code repository available at `https://github.com/STORM-IRIT/scus`. Scatterers are generated according to a settings JSON file with the following format:

```json
{
  "Grid":{
   "Dimension":{
      "x":number, //mm
      "y":number,
      "z":number
   },

      "UseRot":true/false, //random rotation of the cells
      "CellDim":number, //mm
      "SamplesPerCell":number,
      "Sampler":"dart"/"regular"/"uniform"/"cascaded",
      "FixedSeed":number,

      "WeightingObject":{
        "Type: "Sphere",
        "Position":{ //mm
         "x":number,
         "y":number,
         "z":number
      },
        "Radius":number //mm
        }
  },
  "AcquisitionZone":{
   "Dimension":{ //mm
      "Width":number,
      "Height":number,
      "Depth":number
    },

      "Position":{ //mm
```

```
    "x":number,
    "y":number,
    "z":number
  },

  "Rotation":{
    "Angle":number //degree

    "Axis":{ //axis of the rotation, will be normalized
      "x":number,
      "y":number,
      "z":number
      }
    }
  },

  "OutFile":{
    "Mode": "SPACE"/"PROJECTED"/"RAW", // coordinates
    "Name":"... // name of the outfile
  }
}
```

Here, the *WeightingObject* corresponds to the tissue mimicking map and its role is to return the weight for a specific scatterer position during the computation of scatterer amplitudes. It can also be of "Type": "Cube" characterized by "Side" measured in mm, or "Plane", for a medium separated into two by plane at chosen "Height" parameter, Additionally, it can be "Dicom", for medical data but this is not considered for this thesis.

3.2. 3D FEM simulation

In this thesis, tissue behaviour is modeled as linear elastic, isotropic, and nearly incompressible. Tissues are characterized by Young's Modulus (E) and Poisson's Ratio (ν) close to 0.5. Using the FEM, we solve the governing equations of linear elasticity in the discrete domain. In this section we review the proposed deformation model and its implementation using the FEniCS library, in Pyhton [1].

3.2.1 Mathematical Formulation

The equations governing small deformations of a body Ω are given by the kinematic equation (1.2), describing the strain-displacement relationship, the constitutive equation (1.3), describing the stress-strain relationship, and the balance equation (3.1) describing the equilibrium of forces within the body.

From the kinematic and constitutive equations, the relationship between stress and displacement can be derived as:

$$\sigma = \lambda(\nabla \cdot u)I + \mu(\nabla u + (\nabla u)^{\top}) \tag{3.1}$$

The FEM simulation proposed to approximate tissue displacement in the x-, y-, and z-directions under ultrasound probe force involves the following key steps:

Variational Formulation

The variational formulation of Equation (3.1) and Equation (1.5) is formulated as: find $u \in V$ such that:

$$a(u, v) = L(v) \quad \forall v \in \hat{V}, \tag{3.2}$$

where

$$a(u, v) = \int_{\Omega} \sigma(u) : \epsilon(v) \, dx, \tag{3.3}$$

$$\sigma(u) = \lambda(\nabla \cdot u)\mathbf{I} + \mu(\nabla u + (\nabla u)^{\top}) \tag{3.4}$$

$$L(v) = \int_{\Omega} f \cdot v \, dx + \int_{\partial \Omega_T} T \cdot v \, ds. \tag{3.5}$$

Here, $\sigma(u)$ is the stress tensor, $\epsilon(v)$ is the strain tensor, T represents the traction force on the boundary $\partial \Omega_T$. V and $\hat{V}$ are suitable function spaces for the displacement field u and the test function v, respectively.

Domain Discretization

The domain Ω is discretized into tetrahedral elements. A 25x25x25 cube mesh with a resolution of 25 in each dimension is used, resulting in 6x25x25x25 tetrahedral elements. Each element is assigned material properties corresponding to different tissue components or regions within the tissue, allowing for heterogeneous simulations. A subdomain is created specifically for mesh nodes that are in contact with the ultrasound probe, accounting for the localized interaction between the probe and tissue.

Choice of Basis

For our simulation, we use polynomial basis functions of degree 1, suitable for small deformations and linear elasticity to optimize computational efficiency. Each element approximates the displacement field u and force using nodal values and linear shape functions v_k. Thus, the solution u and the force f can be expressed as follows:

$$u = \sum_{k=1}^{n} u_k v_k \quad \text{and} \quad f = \sum_{k=1}^{n} f_k v_k.$$

Assembling the Element Equations

To determine the overall system response modeled by the network of elements, all individual element equations must be assembled. This assembly process combines the matrix equations expressing the behavior of each element into a global system matrix equation that represents the behavior of the entire system. A fundamental aspect of this assembly procedure is that at shared nodes where elements connect, the displacement is the same across all connected elements.

Imposing Boundary Conditions

The Dirichlet boundary condition is employed to represent zero displacement at the bottom face of the cube. The rest of the cube faces are free. Fixed displacement is applied to nodes belonging to the contact area of the probe. Before solving the global system of equations, these fixed nodal values and force loads on known nodes are imposed.

Solving the Global System Equation

A parallel sparse direct solver is employed to solve the global system of equations, integrating boundary conditions and material properties to estimate tissue displacement under ultrasound probe force.

3.2.2 Implementation Details using FEniCS

FEniCS provides a suite of built-in classes and methods that facilitate modeling tasks such as probe-tissue interaction and the creation of diverse subdomains within meshes. Here are the methods from FEniCS used and their specific applications within this work:

- **BoxMesh**: Used to generate a tetrahedral mesh of the tissue sample based on specified grid dimensions.

- **VectorFunctionSpace**: Defines function spaces (V, hatV) for vector-valued functions using continuous piecewise quadratic basis functions of degree 1.

- **MeshFunction**: Associates data with mesh entities such as vertices or cells. It is employed to mark subdomains within the tissue sample volume. This allows for defining different material properties or boundary conditions.

- **SubDomain**: Defines the interface to specify subdomains within a mesh using a MeshFunction. It allows for defining different geometric regions (e.g., cube, sphere, plane) within the tissue sample to simulate various components. The inside() method is used to mark cells belonging to specific subdomains, including defining the contact surface based on the probe's width and height.

- **UserExpression**: Allows for defining custom mathematical vector valuable expressions. We leverage this built-in class to define material properties as functions of space, using the cell basis evaluation. It is also used to model the external force of the probe as a constant load applied uniformly across the contact points belonging to the contact surface subdomain.

- **DirichletBC**: Specifies fixed displacements across parts of the mesh boundaries. Implemented to simulate clamped boundaries by setting zero displacement on the bottom face of the cube.

- **Measure**: Provides integration measures, 'dx' for volume integration across different domains and 'ds' for surface integration. It was used to compute integrals in the weak formulation of PDEs accounting for different subdomains.

- **Solve**: Solves the linear variational problem a(u, v) = L(v) using the MUMPS solver. This step computes the solution for the displacement field u.

The FEM simulation was implemented in Python, consisting of three main components: Volume, Probe, and FEM. The UML class diagram in Figure 3.2, shows their main functionalities and roles in the simulation.

AcquisitionZone_py

- position: np.array
- height: float
- width: float
- depth: float
- rotation_angle : float
- rotation_axis: np.array
- rotation: Rotation
- qx2, qy2, qz2, qw2: float
- dqxqy, dqwqz, dqxqz, dqwqy,
  dqyqz, dqwqx: float

+ __init__(az_settings: dict)
+ update_az(az_settings: dict)
+ setRotation() : void
+ isInside(point: np.array) : bool
+ projectPoint(point: np.array) : np.array

Extends

Volume

- dim: dict
- cellDim: float
- mesh: Mesh
- mu_values: list[float]
- lmda_values: list[float]
- E_values: list[float]
- bc_dict: dict
- subdomains: MeshFunction
- boundary_markers: MeshFunction

+ __init__(grid_settings: dict)
+ createMesh() : Mesh
+ setSubdomains() : void
+ mark_boundaries(probe) : void
+ setBoundaryCondition(probe_position) :
+ boundary(x, on_boundary) : bool
+ saveMaterials(filename) : void

Probe

- direction: tuple
- force: Force

+ __init__(az_settings_dict: dict, force_magnitude: float)
+ getDirection() : tuple
+ isContactSurface(x, on_boundary) : bool

Use

Use

FEM

- volume: Volume
- probe: Probe
- V: VectorFunctionSpace
- mu: mu
- lbda: lmda
- bc: DirichletBC
- dx : Measure
- dxNum: int
- ds: Measure

+ __init__(volume, probe)
+ epsilon(u) : Expression
+ sigma(u): Expression
+ traction(u): Expression
+ solve(): Function

Figure 3.2: UML Class Diagram for FEM simulation main components: Volume, Probe and FEM. Note AcquisitionZone_py, shown in blue, corresponds a modified version of the original AquisitionZone class in C++

3.3. Ultrasound simulation combining SCUS and 3D FEM

In order to incorporate tissue displacement in the simulation framework, two modifications are introduced to the simulation parameters initially described in subsection 3.1.3. Firstly, the incorporation of the field "Force", corresponds to the magnitude of the external force corresponding to the probe's pushing force in Newtons (N). Secondly, a *WeightingObject* of "Type": "Phantom". This new type includes a collection of simple *WeightingObject* of the type cube, sphere, and plane, that can be used to create anatomical phantoms at the elementary level or to simulate different components within tissues according to biomechanical parameters. Here, is an example.

```
{
  "WeightingObject"{
      "Type": "Phantom",
      "GeomObj": [
      {
         "Type: "Sphere"/"Cube"/"ThickPlane",
         "Position":{ //mm
         "x":number,
         "y":number,
         "z":number
         },
         "Size": value //radius, side, thickness
         "Value": value //weight
         "E": value //Young's Modulus
         "nu": value //Poisson's Ratio
      },

      {
         //another object
      },

      {
          //another object

      }
      ]
}
```
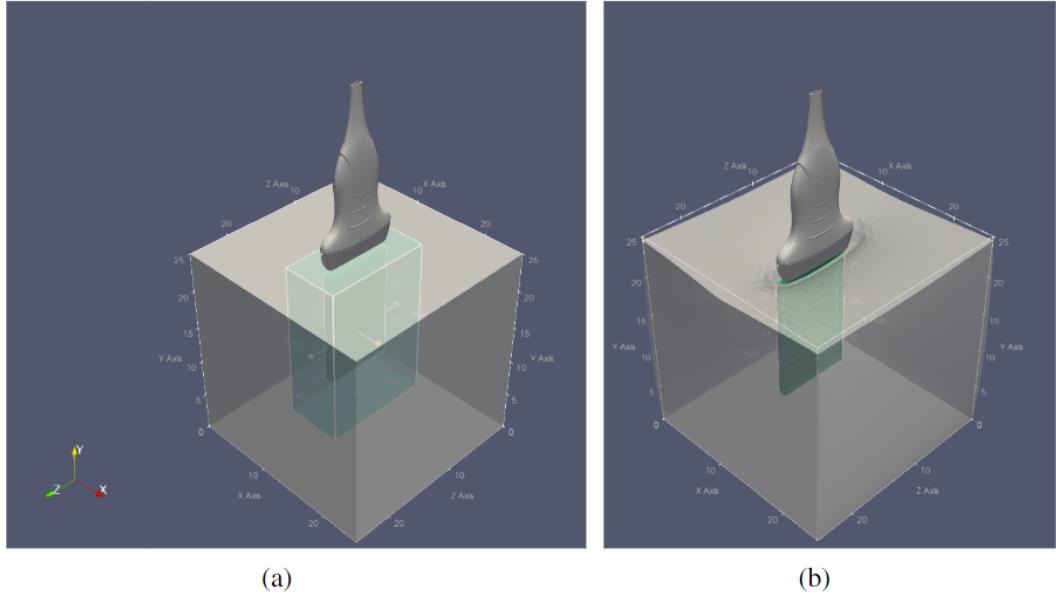
Figure 3.3: (a) Augmented Acquisition Zone in the reference configuration. (b) Acquisition Zone in the deformed configuration. Due to the compression force of the probe, tissues deform, allowing the probe to approach the internal anatomy and cover deeper areas.

Following the simulation workflow proposed in Figure 3.1, we can summarize the integration of the deformation model and the scatterer model as a sequential process with the following steps.

1. **Compute Displacement Field**: The displacement field u, resulting from the force of the probe on a tissue-mimicking volume (with given E and ν), is computed by the deformation model using the 3D FEM.

2. **Update Initial AZ Dimension**: Adjust the initial AZ dimensions in the simulation settings, accounting for the maximum displacement in the x, y, and z directions as $AZ(\pm|u.\text{max}()|)$, see Figure 3.3(a). The scatterer model, using simulation parameters and "Mode": "SPACE", generates scatterers in a grid coordinate system with respect to the augmented AZ.

3. **Update Scatterers**: Modify the scatterers' positions, with their corresponding amplitudes, according to the displacement field to reflect the tissue deformation. As a result, scatterers will lie within the deformed configuration of the tissue sample.

4. **Update Initial AZ Position**: Adjust the initial AZ position to simulate the probe's displacement into the tissues when a pushing force is applied. The new AZ

position in the deformed configuration, p_{def}, is computed as follows:

$$p_{\text{def}} = p_{\text{ref}} + |u(p_{\text{ref}})| \odot d$$

where p_{ref} corresponds to the initial position of the acquisition zone (x, y, z), $u(p_{\text{ref}})$ represents the displacement (in mm) of p_{ref}, $\odot$ denotes element-wise multiplication, and d is the direction vector given by the rotation of the probe.

5. **Filter Scatterers**: Filter the scatterers based on their positions with respect to the AZ in the deformed configuration, see Figure 3.3(b).

The simulation is run in Python, the scatterers are generated using an executable file run as a Python subprocess.

3.4. B-mode ultrasound image generation

Following Gaits et al.(2023), a convolutional approach is used to generate the final ultrasound slice from the displaced scatterers. Scatterers lying in the AZ post- deformation, are projected into the probe coordinate system and discretized into a 2D scatterer map. Each scatterer's amplitude contributes to this map by summing its amplitude into its closest pixel. The resulting scatterer map is then convolved with a spatially-invariant Point Spread Function (PSF) to simulate the ultrasound image.

3.5. Conclusion

In this chapter, we explored the integration of tissue displacement within the ultrasound simulation framework. We proposed updating scatterers with displacements obtained from 3D FEM simulations, driven by external forces from the probe and a tissue-mimicking volume characterized by Young's modulus (E) and Poisson's ratio (ν). There are two key limitations in directly applying displacement to scatterers in a reference configuration: it neglects out-of-plane deformations, and scatterers corresponding to above the probe's AZ are disregarded. To address these limitations, we propose generating scatterers relative to an augmented acquisition zone, applying the correspondent displacement, and finally employing filtering techniques to extract only those scatterers within the probe's field of view in the deformed configuration. The use of FEniCS allowed for easy integration and provided versatility to adapt the modeling to our specific problem.

Chapter 4

Results

4.1.   Deformation in Homogeneous vs Non-Homogeneous Tissue Samples

4.1.1   Experimental setup and FE Models

Axial compression is applied by vertically displacing the probe into the tissue, see Figure 4.2. An incremental force, ranging from 0 to 1.5N, is applied in the negative y direction. The results are evaluated at probe displacements of 0 mm, 2.5 mm, and 4.5 mm. Two types of tissue samples are modeled: homogeneous and non-homogeneous. We use the term "non-homogeneous" to refer to variations in biomechanical properties between different tissue components, but note each component remains modeled as a linear, homogeneous, and incompressible tissue. Table 4.1 defines the size, position, and biomechanical properties of the tissue components. Additionally, it includes the echogenic values, where small inclusions are treated as high echogenic mediums.

For the scatterer model generation, the following parameters are used: UseRot = true, SamplesPerCell = 27, Sampler = "dart", and FixedSeed = 19011998. The acquisition zone dimensions are Width : 12, Height : 1, Depth : 15, positioned at x : 12.5, y : 25, z : 12.5, with a rotation of Angle : −90, Axis : x : 0, y : 0, z : 1. B-mode ultrasound images are generated with a resolution proportional to the width and depth dimensions of the acquisition zone, using 120, and 150 for the lateral and axial resolution.
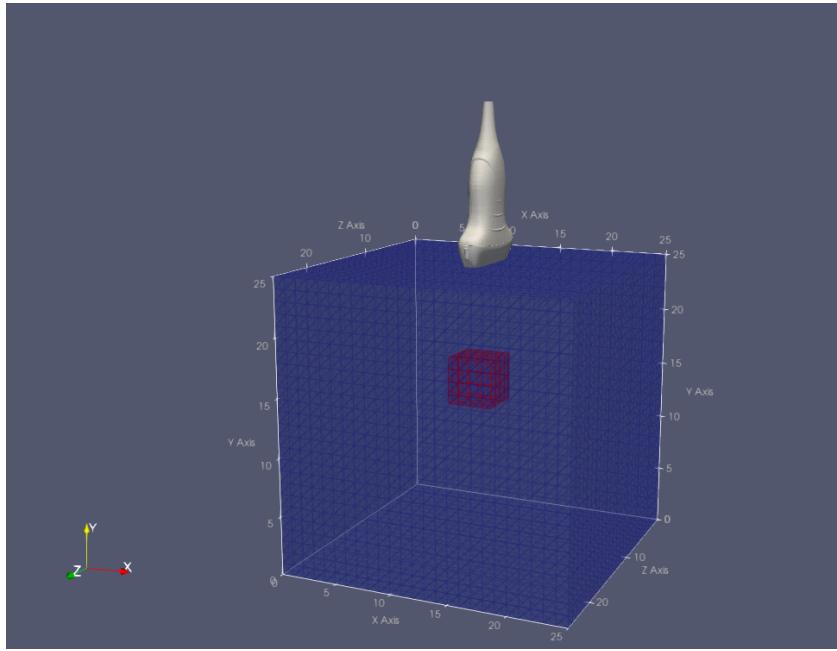
Figure 4.2: FE model to study homogeneous vs non-homogeneous tissue deformation. The force is applied in the -y direction to the nodes of the mesh in contact with the surface of the linear array probe. The bottom face of the cube is clamped. For a non-homogeneous tissue sample, the mechanical properties of the incision (small cube) differ from the surrounding tissue.

Object	Size (mm)	Position (mm)	Value	E (kPa)	ν
Cube	25	(12.5, 12.5, 12.5)	1	0.05	0.49
Cube	4	(12.5, 12.5, 12.5)	10	0.05	0.49

(a) Homogeneous tissue sample

Object	Size (mm)	Position (mm)	Value	E (kPa)	ν
Cube	25	(12.5, 12.5, 12.5)	1	0.05	0.49
Cube	4	(12.5, 12.5, 12.5)	10	0.5	0.49

(b) Non-Homogeneous tissue sample

Figure 4.1: FE Model Parameters for Homogeneous and Non-Homogeneous Tissue Samples. The non-homogeneous sample includes a hard inclusion 10 times stiffer than the surrounding tissue.

4.1.2 Qualitative assessment of results

Deformation in B-mode image

Figure 4.3 shows the simulated 2D slices under different probe positions. In (a) the probe is placed on the tissue surface. In (b) and (c), the probe is pushed into the tissue by 2.5 mm and 4.5 mm, respectively. The top row corresponds to simulations without considering tissue deformation, where the image is directly generated from scatterers extracted from a reference configuration. The second and third rows show slices incorporating tissue deformation from 3D FEM simulations accounting for the mechanical properties of the homogeneous and non-homogeneous tissue samples, respectively.

Differences in the position of the small cube relative to the probe (top edge of the image) are evident, with a smaller distance observed when no deformation model is considered. This discrepancy becomes more pronounced with increased compression force. The tissue responds to the applied force by undergoing displacement and compression, not only noticeable in the cube but also in the surrounding tissue. Although the displacement in the vertical direction seems comparable for both cubes, the non-homogeneous sample offers greater resistance to compression due to its stiffer inclusion in the middle.
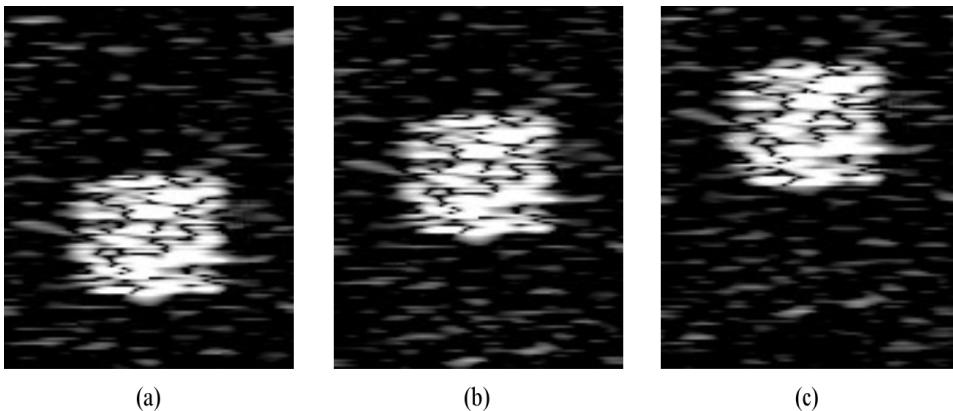
3D deformation of tissue samples

3D visualization allows for the observation of displacement and deformation in all directions, providing better insights. Figure 4.4 shows the magnitude of the displacement field vectors from FEM simulations for homogeneous (a) and non-homogeneous (b) tissue samples under two different probe displacements. The magnitude of the displacement vector indicates how far each point is displaced due to the applied force. Larger magnitudes are shown in red, while lesser displacement is shown in blue.
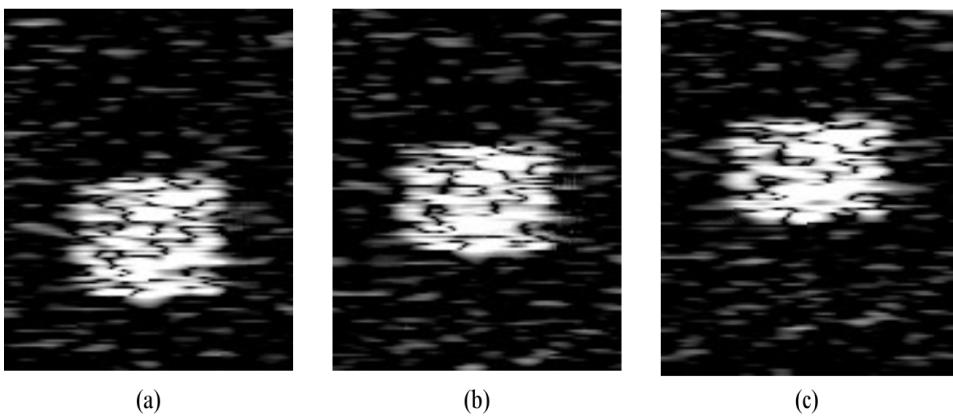
Greater displacement occurs at points in contact with the probe and then decreases progressively from the contact points. In the homogeneous medium, the displacement decreases uniformly through both subdomains. In contrast, the non-homogeneous tissue sample exhibits a non-uniform displacement pattern. Points belonging to the small cube subdomain, experience a lower displacement due to its increased rigidity. This results in less compression of the small cube, and a higher force to achieve the same probe displacement compared to the homogeneous tissue sample.

In Figure 4.5, we visualize the effects of applying the estimated displacement field to

No Tissue Deformation

(a) (b) (c)

Tissue Deformation in Homogeneous Tissue Sample

(a) (b) (c)

Tissue Deformation in Non-Homogeneous Tissue Sample


(a) (b) (c)
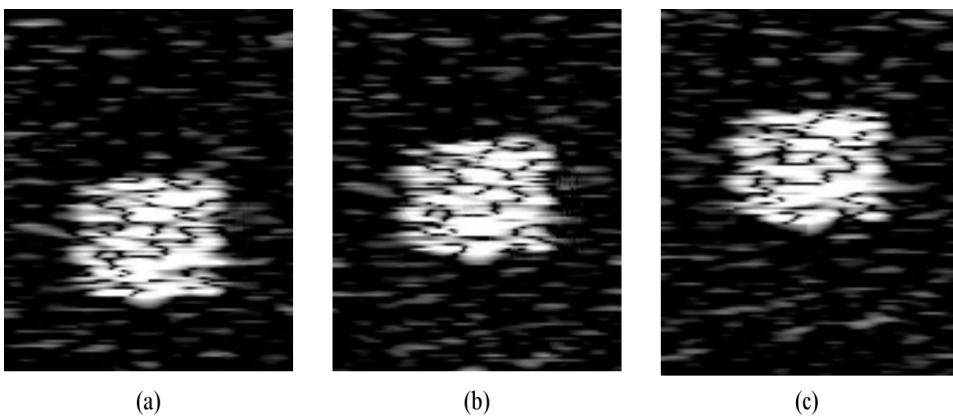
Figure 4.3: Simulation of B-mode images using probe displaced by (a) 0 mm, (b) 2.5mm, and (c) 4.5 mm into the tissue samples. The first row shows the output from previous work. The second and third rows illustrate the results incorporating tissue deformation in the simulation framework for homogeneous and non-homogeneous tissue samples, respectively.

(a)

(b)
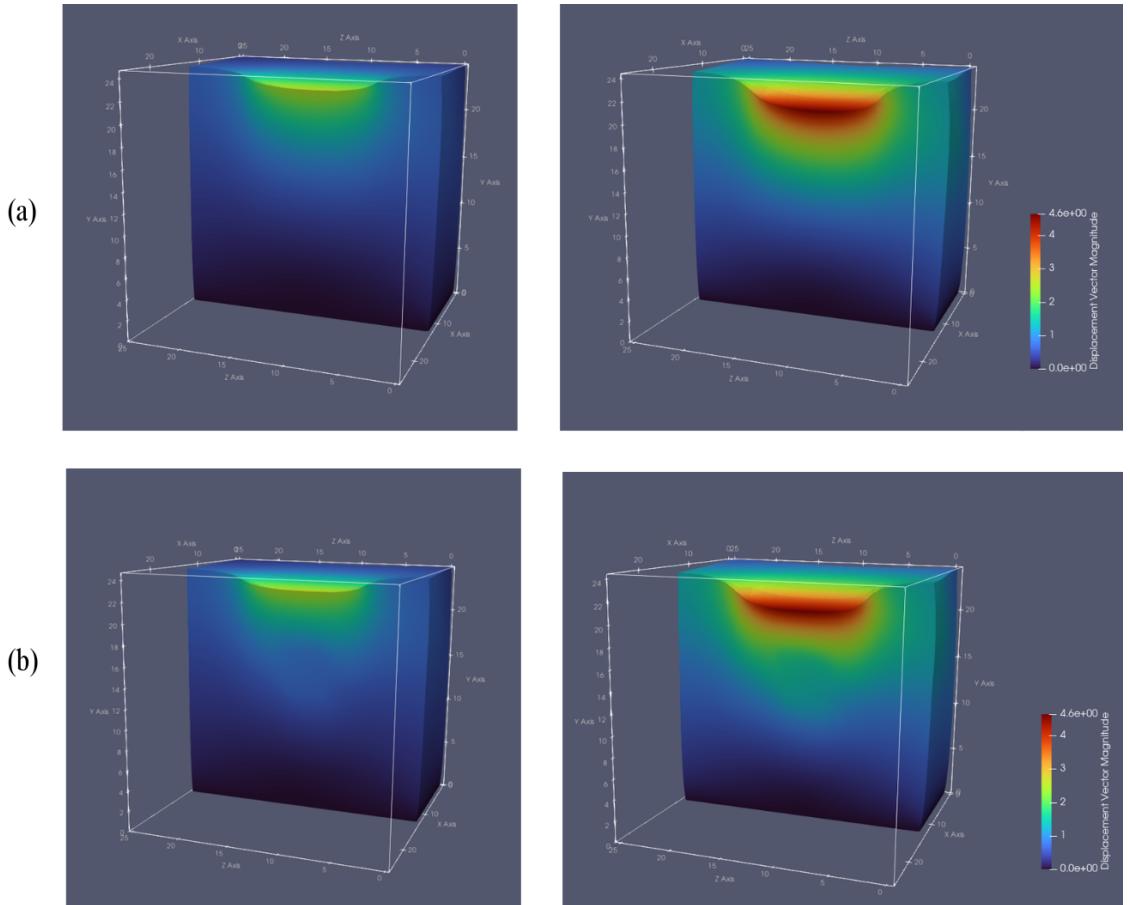
Figure 4.4: Magnitude of displacement vector from FEM simulation. Red values indicate areas with larger displacement, typically near the probe. The first column shows deformation from a 2.5 mm probe displacement, requiring 0.55 N for the (a)homogeneous and 0.57 N for the (b) non-homogeneous tissue. The second column shows deformation from a 4.5 mm probe displacement, requiring 0.99 N and 1.05 N respectively.

mesh nodes, achieving the deformed configurations corresponding to a probe displacement of 5 mm. This comparison highlights the deformation effects in homogeneous and non-homogeneous tissue samples. In the homogeneous medium, both displacement and changes in the curvature of the top face are observed due to the external force. Conversely, in the non-homogeneous tissue sample, the small cube is displaced relative to the reference configuration, but the curvature changes are not apparent.


No Tissue Deformation   **Tissue Deformation in Homogeneous Sample**   **Tissue Deformation in Non Homogeneous Sample**
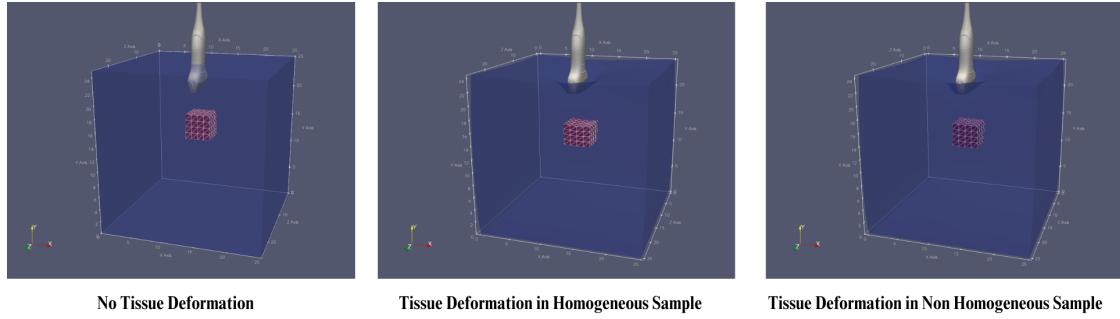
Figure 4.5: Visualization of (a) reference and (b)-(c) deformed configurations as reults of probe displacement of 4.5 mm. The homogeneous tissue sample (b) exhibits uniform displacement throughout both subdomains, with noticeable changes in curvature on the top face of the small cube in response to the external force. In the non-homogeneous sample (c), the stiffer properties of the cube make it more resistant to deformation.

4.1.3   Quantitative assessment of results

Probe-to-inclusion distance

Figure 4.6, shows the annotated B-mode images with the corresponding distance from the probe to the small cube when the probe reaches a displacement of 4.5 mm. Confirming the displacement and compression of the cube observed from the qualitative evaluation.

Effect of deformation on scatterer spatial distribution

Figure 4.8, shows the count of 1 mm^3 cells within the acquisition zone of a probe displaced 4.5mm, each cell corresponding to a 10x10 pixel square in the generated image. The mean and standard deviation of the scatterer count distribution, calculated using a mixture of Gaussian distributions, are reported in Table 4.7, along with the corresponding compression force and total scatterer count per image. When considering deformation,

(a)   (b)   (c)
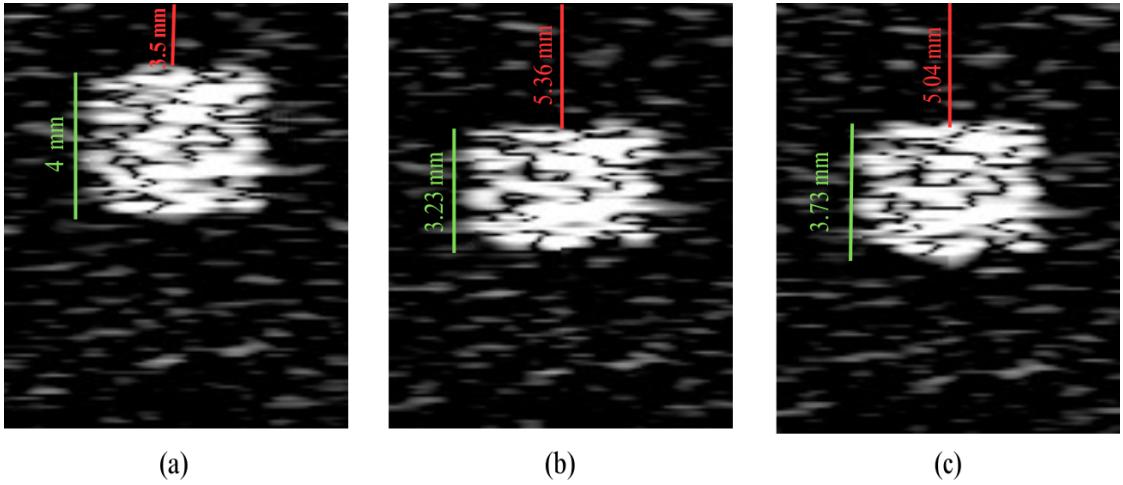
Figure 4.6: Distance cube to probe (red) and length of the small cube (green) for (a) no deformation, (b) deformation in a homogeneous and (b) deformation in a non-homogeneous tissue sample, using a probe displacement of 4.5mm

the applied displacement disrupts their uniform count. As a result, the total number of samples per cell within the acquisition zone deviates from the original count of 27.

Configuration	Force	Scatterers count	
	(N)	total	grid cell
Reference	-	4858	$27.0 \pm 0.0, 13.5 \pm 0.96$
Homogeneous	0.55	4952	$27.7 \pm 2.62, 13.17 \pm 3.98$
Non-Homogeneous	0.57	4924	$27.59 \pm 2.61, 12.43 \pm 3.18$

(a) 2.5 mm

Configuration	Force	Scatterers count	
	(N)	total	grid cell
Reference	-	4858	$27.0 \pm 0.0, 12.96 \pm 2.15$
Homogeneous	0.99	5109	$28.54 \pm 3.33, 13.04 \pm 2.88$
Non-Homogeneous	1.05	5117	$28.67 \pm 3.45, 12.61 \pm 2.77$

(b) 4.5 mm

Figure 4.7: comparison of scatterer counts and applied forces for different configurations at two probe displacements: 2.5 mm and 4.5 mm
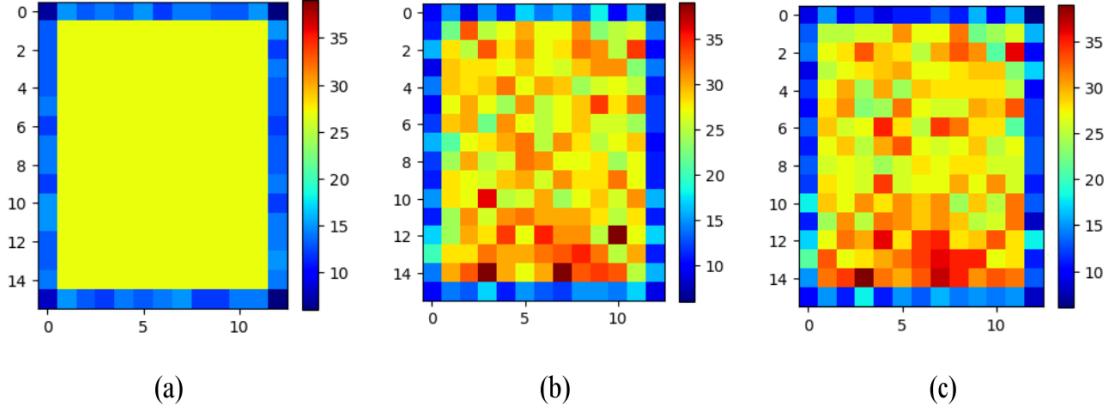
Figure 4.8: Grid cell scatterer counts within the 1 mm³ acquisition zone for a probe displacement of 4.5 mm in (a) reference configuration, and (b)-(c) in deformed configuration for a homogeneous and non-homogeneous sample, respectively. Increased counts at the borders indicate partial cell occlusion. Central cell count is no longer uniform post-deformation.

4.2. Breast Mimicking Tissue Sample

4.2.1 Experimental setup and FE Models

The same parameters were used for scatterer generation, and axial compression was similarly applied by vertically displacing the probe into the tissue. An incremental force ranging from 0 to 1.5 N was applied in the negative y direction. We evaluate the results using probe displacements of 0 mm, 2.5 mm, and 4.5 mm. A phantom is constructed with mechanical properties mimicking various tissue components of the breast, reported in the literature [39]. The FE model is shown in Figure 4.10.

Object	Component	Size (mm)	Position (mm)	Value	E (kPa)	ν
ThickPlane	Skin	1	(12.5, 25, 12.5)	100	200	0.49
ThickPlane	Fat	1	(12.5, 24, 12.5)	5	1.5	0.49
Cube	Soft Tissue	25	(12.5, 12.5, 12.5)	20	10	0.49
Sphere	Tumor	2	(12.5, 12.5, 12.5)	3	40	0.49

Figure 4.9: FE Model parameters to simulate B-mode images of breast tissue with tumor.
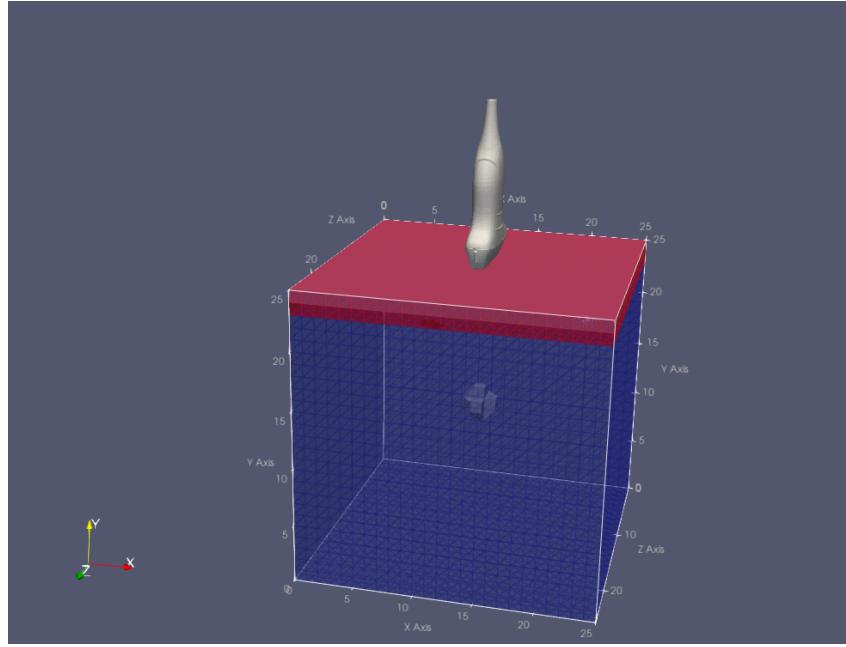
Figure 4.10: FE model of a sample with multiple layers (skin and fat) above the inclusion (tumor) and soft tissue with breast mechanical properties. The force is applied in the -y direction to the nodes of the mesh in contact with the surface of the linear array probe. The bottom face of the cube is clamped.

4.2.2 B-mode image simulation results

Figure 4.9 shows the simulated images obtained with probe displacements of 2.5mm and 4.5 mm, comparing scenarios with and without tissue deformation. In the absence of deformation, tissue domains above the probe position are not captured. However, incorporating tissue displacement accounts for compression at the top layers, resulting in a more realistic simulation. The simulation of a B-mode image with tissue deformation, takes on average less than 18s, with the modeling phase comprising approximately 16s of this duration.

4.3. Conclusion

In this chapter we showed the results of introducing tissue deformation to obtain more realistic B-mode ultrasound images, contrasting them with their non-deformed counterparts. By accounting for deformation, simulations can reflect tissue behavior under probe compression, mimicking real-world examination. We showed the deformation effects at both a pixel level and scatterer level and used 3D visualization to analyze tissue responses in both in-plane and out-of-plane directions under probe force. Finally, we demonstrated

No Tissue Deformation

(a)　　　　　　　(b)　　　　　　　(c)

Incorporating Tissue Deformation

(a)　　　　　　　(b)　　　　　　　(c)
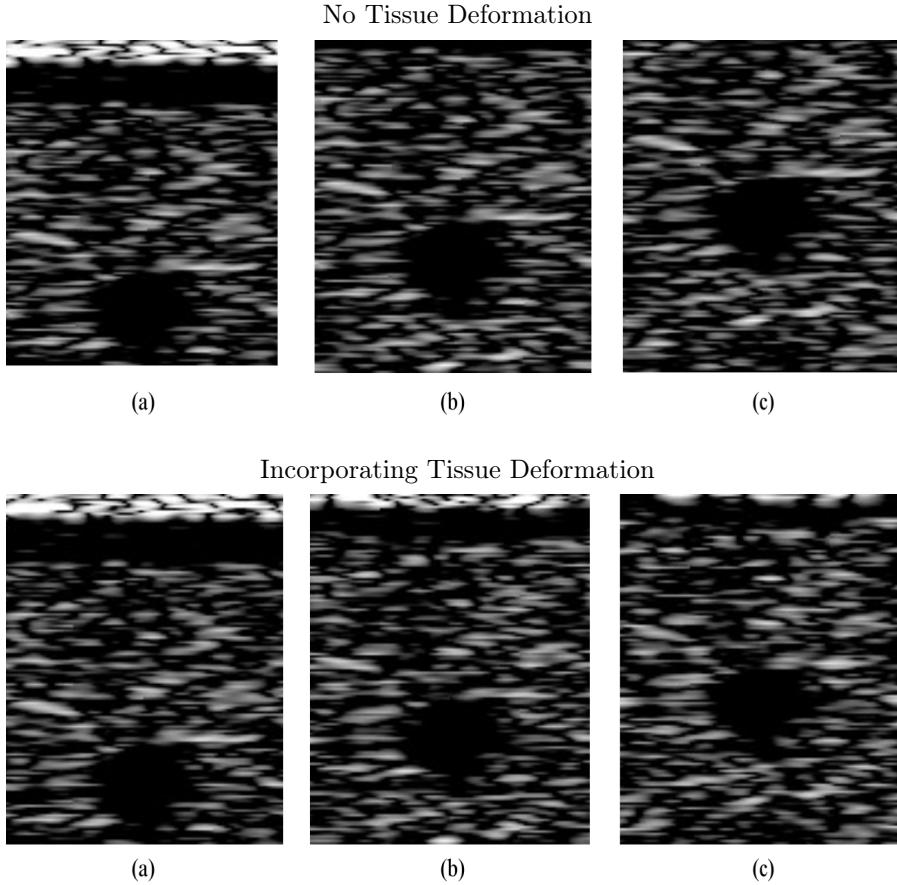
Figure 4.11: Simulation of B-mode images at different probe positions (a) surface of a tissue sample, and probe with displacement (b) 2.5 mm and (c)4.5mm. Tissue properties for breast components are used to represent soft tissue, tumor, skin, and fat. Skin and fat, are modeled as layers of 1mm, while the tumor is represented by a sphere with a radius of 2 mm. The top row corresponds to simulation results using previous work. The second row shows a more realistic simulation by incorporating the deformation of the tissues.

an example using the Phantom WeightingObject to replicate various tissue components, such as layers or spheres, to simulate tumors within a sample with breast tissue mechanical properties.

Chapter 5

Summary

5.1. Problem statement

Integrating tissue deformation into ultrasound simulation is a crucial step towards achieving more realistic ultrasound images, which can greatly enhance medical training and ultrasound technology development. This involves accounting for anatomical deformations caused by the pushing force applied by the probe before image acquisition.

The primary objective of this thesis was to achieve a more realistic simulation of ultrasound images by incorporating the deformation of soft tissues into an existing ultrasound simulator, which was able to extract scatterers from a tissue-mimicking volume represented as a regular, non-deformed grid.

In this work, we proposed to estimate the positions of the scatterers in the deformed configuration by updating their positions with the displacement field obtained through the solution of linear elasticity equations using the Finite Element Method. This approach inherently accounts for tissue properties, such as stiffness and compressibility. Furthermore, only scatterers within the probe acquisition zone in the deformed configuration are considered for image generation, aligning with clinical practice where only anatomical structures within the probe's field of view contribute to the final ultrasound image.

5.2. Results

The results closely aligned with our initial expectations, demonstrating the coherence and meaningfulness of the generated images. A comparative analysis was conducted

between simulations performed without tissue deformation and those incorporating deformation, considering both homogeneous and non-homogeneous tissue samples. When disregarding deformation, the upper layers of tissues were absent in the final image, and the modeled anatomy appeared closer to the probe surface.

The simulation framework enabled the creation of diverse phantoms with simple geometrical shapes, mimicking various tissue components such as those found in breast tissue. Incorporating rigid inclusions, for instance, facilitated the simulation of tumors. FEniCS' adaptability in defining custom mesh subdomains and its robust solver capabilities made it an adequate choice for accurately modeling interactions probe-tissue interactions.

An important aspect to note was the perturbation in scatterer spatial distribution, resulting in deviations from the original count per cell. Some scatterers exited the acquisition zone when the displacement field was applied, particularly as the side faces of the cube allowed free displacement. Users should use adequate parameters for scatterers per cell to ensure the development of fully formed speckle patterns.

However, it is essential to acknowledge the computational cost associated with our approach. While ultrasound simulation is characterized by its real-time capability, solving the displacement field introduced a notable delay. On average, processing a cube of $25m^3$ took approximately 16 seconds, compared to less than 2 seconds for a slice without deformation.

5.3.   Future plans

In our future plans, we aim to explore alternative modeling techniques that offer lower computational costs compared to FEM in order to ensure compatibility with real-time capabilities.

Bibliography

[1] M. Alnæs, J. Blechta, J. Hake, *et al.*, "The fenics project version 1.5," *Archive of numerical software*, vol. 3, no. 100, 2015.

[2] J. Shriki, "Ultrasound physics," *Critical care clinics*, vol. 30, no. 1, pp. 1–24, 2014.

[3] J. W. Hunt, A. E. Worthington, and A. T. Kerr, "The subtleties of ultrasound images of an ensemble of cells: Simulation from regular and more random distributions of scatterers," *Ultrasound in medicine & biology*, vol. 21, no. 3, pp. 329–341, 1995.

[4] J. A. Jensen, "Field: A program for simulating ultrasound systems," *Medical & Biological Engineering & Computing*, vol. 34, no. sup. 1, pp. 351–353, 1997.

[5] D. Garcia, "Simus: An open-source simulator for medical ultrasound imaging. part i: Theory & examples," *Computer Methods and Programs in Biomedicine*, vol. 218, p. 106 726, 2022.

[6] J. Meunier and M. Bertrand, "Ultrasonic texture motion analysis: Theory and simulation," *IEEE transactions on medical imaging*, vol. 14, no. 2, pp. 293–300, 1995.

[7] H. Gao, H. F. Choi, P. Claus, *et al.*, "A fast convolution-based methodology to simulate 2-dd/3-d cardiac ultrasound images," *IEEE transactions on ultrasonics, ferroelectrics, and frequency control*, vol. 56, no. 2, pp. 404–409, 2009.

[8] Q. Wang, B. Peng, Z. Cao, X. Huang, and J. Jiang, "A real-time ultrasound simulator using monte-carlo path tracing in conjunction with optix engine," in *2020 IEEE International Conference on Systems, Man, and Cybernetics (SMC)*, IEEE, 2020, pp. 3661–3666.

[9] M. F. Insana and T. J. Hall, "Parametric ultrasound imaging from backscatter coefficient measurements: Image formation and interpretation," *Ultrasonic imaging*, vol. 12, no. 4, pp. 245–267, 1990.

[10] V. M. Narayanan, P. Shankar, and J. M. Reid, "Non-rayleigh statistics of ultrasonic backscattered signals," *IEEE transactions on ultrasonics, ferroelectrics, and frequency control*, vol. 41, no. 6, pp. 845–852, 1994.

[11] F. Gaits *et al.*, "Efficient stratified 3d scatterer sampling for freehand ultrasound simulation," *IEEE Transactions on Ultrasonics, Ferroelectrics, and Frequency Control*, 2023.

[12] D. Garcia, "Make the most of must, an open-source matlab ultrasound toolbox," in *2021 IEEE international ultrasonics symposium (IUS)*, IEEE, 2021, pp. 1–4.

[13] J. Zhang, Y. Zhong, and C. Gu, "Deformable models for surgical simulation: A survey," *IEEE reviews in biomedical engineering*, vol. 11, pp. 143–164, 2017.

[14] G. Irving, C. Schroeder, and R. Fedkiw, "Volume conserving finite element simulations of deformable models," *ACM Transactions on Graphics (TOG)*, vol. 26, no. 3, 13–es, 2007.

[15] R. Chen, L. Chen, and S. Parashar, "Gaps: Geometry-aware, physics-based, self-supervised neural garment draping," *arXiv preprint arXiv:2312.01490*, 2023.

[16] W. Maurel, D. Thalmann, Y. Wu, and N. M. Thalmann, *Biomechanical models for soft tissue simulation*. Springer, 1998, vol. 48.

[17] R. M. Sigrist, J. Liau, A. El Kaffas, M. C. Chammas, and J. K. Willmann, "Ultrasound elastography: Review of techniques and clinical applications," *Theranostics*, vol. 7, no. 5, p. 1303, 2017.

[18] M. M. Doyley, "Model-based elastography: A survey of approaches to the inverse elasticity problem," *Physics in Medicine & Biology*, vol. 57, no. 3, R35, 2012.

[19] Wolfram Research, *Structural mechanics: Solid mechanics*, `https://reference.wolfram.com/language/PDEModels/tutorial/StructuralMechanics/SolidMechanics.html`, Accessed on: 2024-05-23.

[20] L. CHEN, "Introduction to linear elasticity,"

[21] A. S. Kashani and M. Packirisamy, "Cancer cells optimize elasticity for efficient migration," *Royal Society Open Science*, vol. 7, no. 10, p. 200 747, 2020.

[22] S. Budday, T. C. Ovaert, G. A. Holzapfel, P. Steinmann, and E. Kuhl, "Fifty shades of brain: A review on the mechanical testing and modeling of brain tissue," *Archives of Computational Methods in Engineering*, vol. 27, pp. 1187–1230, 2020.

[23] M. Freutel, H. Schmidt, L. Dürselen, A. Ignatius, and F. Galbusera, "Finite element modeling of soft tissues: Material models, tissue interaction and challenges," *Clinical Biomechanics*, vol. 29, no. 4, pp. 363–372, 2014.

[24] T.-N. Nguyen, M.-C. Ho Ba Tho, and T.-T. Dao, "A systematic review of real-time medical simulations with soft-tissue deformation: Computational approaches, interaction devices, system architectures, and clinical validations," *Applied Bionics and Biomechanics*, vol. 2020, no. 1, p. 5 039 329, 2020.

[25] H. Delingette, "Toward realistic soft-tissue modeling in medical simulation," *Proceedings of the IEEE*, vol. 86, no. 3, pp. 512–523, 1998.

[26] M. Schlaikjer, S. Petersen, J. A. Jensen, and P. F. Stetson, "Tissue motion in blood velocity estimation and its simulation," in *1998 IEEE Ultrasonics Symposium. Proceedings (Cat. No. 98CH36102)*, IEEE, vol. 2, 1998, pp. 1495–1499.

[27] M. Schlaikjer, S. Torp-Pedersen, and J. A. Jensen, "Simulation of rf data with tissue motion for optimizing stationary echo canceling filters," *Ultrasonics*, vol. 41, no. 6, pp. 415–419, 2003.

[28] P. Chaturvedi, M. F. Insana, and T. J. Hall, "2-d companding for noise reduction in strain imaging," *IEEE transactions on ultrasonics, ferroelectrics, and frequency control*, vol. 45, no. 1, pp. 179–191, 1998.

[29] R. G. Lopata, M. M. Nillesen, H. H. Hansen, I. H. Gerrits, J. M. Thijssen, and C. L. De Korte, "Performance evaluation of methods for two-dimensional displacement and strain estimation using ultrasound radio frequency data," *Ultrasound in medicine & biology*, vol. 35, no. 5, pp. 796–812, 2009.

[30] A. Al-azawi and J. Soraghan, "Dynamic ultrasound scatterer simulation model using field-ii and fem for speckle tracking," *International Journal of Biomedical and Biological Engineering*, vol. 7, no. 9, pp. 589–593, 2013.

[31] Z. Hosseini, A. Khadem, and M. H. Bibalan, "Displacement estimation for ultrasound elastography based on a robust uniform stretching method," in *2022 30th International Conference on Electrical Engineering (ICEE)*, IEEE, 2022, pp. 791–795.

[32] M. T. Islam, S. Tang, C. Liverani, S. Saha, E. Tasciotti, and R. Righetti, "Noninvasive imaging of young's modulus and poisson's ratio in cancers in vivo," *Scientific reports*, vol. 10, no. 1, p. 7266, 2020.

[33] E. Tagliabue, D. Dall'Alba, E. Magnabosco, I. Peterlik, and P. Fiorini, "Biomechanical modelling of probe to tissue interaction during ultrasound scanning," *International Journal of Computer Assisted Radiology and Surgery*, vol. 15, pp. 1379–1387, 2020.

[34] B. Flack, M. Makhinya, and O. Goksel, "Model-based compensation of tissue deformation during data acquisition for interpolative ultrasound simulation," in *2016 IEEE 13th international symposium on biomedical imaging (ISBI)*, IEEE, 2016, pp. 502–505.

[35] O. Goksel and S. E. Salcudean, "B-mode ultrasound image simulation in deformable 3-d medium," *IEEE transactions on medical imaging*, vol. 28, no. 11, pp. 1657–1669, 2009.

[36] R. Starkov, L. Zhang, M. Bajka, C. Tanner, and O. Goksel, "Ultrasound simulation with deformable and patient-specific scatterer maps," *International journal of computer assisted radiology and surgery*, vol. 14, pp. 1589–1599, 2019.

[37] R. Starkov, C. Tanner, M. Bajka, and O. Goksel, "Ultrasound simulation with animated anatomical models and on-the-fly fusion with real images via path-tracing," *Computers & Graphics*, vol. 82, pp. 44–52, 2019.

[38] Y. Huang, L. Yu, and F. Zhang, "A survey on puncture models and path planning algorithms of bevel-tipped flexible needles," *Heliyon*, 2024.

[39] M. T. Reza, A. H. M. M. Kamal, M. R. H. Khan, and M. R. Islam, "Young's modulus distribution prediction analysis of elasticity imaging technique based on location of tumors," *INTERNATIONAL JOURNAL OF COMPUTER SCIENCE AND NETWORK SECURITY*, vol. 18, no. 8, pp. 112–117, 2018.